JOURNAL OF GEOPHYSICAL RESEARCH, VOL. 116, C00H05, doi:10.1029/2011JC007278, 2011

Polarized light field under dynamic ocean surfaces: Numerical modeling compared with measurements

Yu You,[1] George W. Kattawar,[1] Kenneth J. Voss,[2] Purushottam Bhandari,[2] Jianwei Wei,[3] Marlon Lewis,[3,4] Christopher J. Zappa,[5] and Howard Schultz[6]

Received 10 May 2011; revised 10 July 2011; accepted 18 July 2011; published 14 October 2011.

[1] As part of the Radiance in a Dynamic Ocean (RaDyO) program, we have developed a numerical model for efficiently simulating the polarized light field under highly dynamic ocean surfaces. Combining the advantages of the three-dimensional Monte Carlo and matrix operator methods, this hybrid model has proven to be computationally effective for simulations involving a dynamic air-sea interface. Given water optical properties and ocean surface wave slopes obtained from RaDyO field measurements, model-simulated radiance and polarization fields under a dynamic surface are found to be qualitatively comparable to their counterparts from field measurements and should be quantitatively comparable if the light field measurement and the wave slope/water optical property measurements are appropriately collocated and synchronized. This model serves as a bridge to connect field measurements of water optical properties, wave slopes and polarized light fields. It can also be used as a powerful yet convenient tool to predict the temporal underwater polarized radiance in a real-world situation. When appropriate surface measurements are available, model simulation is shown to reveal more dynamic features in the underwater light field than direct measurements.

Citation: You, Y., G. W. Kattawar, K. J. Voss, P. Bhandari, J. Wei, M. Lewis, C. J. Zappa, and H. Schultz (2011), Polarized light field under dynamic ocean surfaces: Numerical modeling compared with measurements, *J. Geophys. Res.*, *116*, C00H05, doi:10.1029/2011JC007278.

1. Introduction

[2] The polarized light field in the ocean has been the subject of extensive research for a diversity of purposes such as marine biology, remote sensing, and underwater imaging. The polarized light field in the surface boundary layer is especially important, as it is primarily determined by the highly dynamic air-sea interface and is believed to contain useful information about the interface. The Radiance in a Dynamic Ocean (RaDyO) project was designed to investigate the relation between the time-dependent light field distribution and the surface boundary layer (SBL), to construct a model to relate the two, and to explore the feasibility of reconstructing the SBL conditions from light field measurements. In this context, understanding the light field, including its polarization state, immediately beneath the air-sea interface is of great importance.

[3] There are basically two approaches to study the polarized light field in the ocean. Field measurement is a straightforward approach if one has appropriate measuring techniques and equipment. Measurements of the underwater polarized light field date back to *Waterman* [1954] and *Waterman and Westell* [1956], followed by *Ivanoff et al.* [1961] and *Timofeeva* [1974]. Some recent efforts include *Cronin and Shashar* [2001], *Shashar et al.* [2004], *Sabbah et al.* [2006], and *Sabbah and Shashar* [2006, 2007]. All of these measurements have been performed either at relatively large depths where effects of the dynamic surface are negligible or under a relatively flat surface, such that the polarized light field is largely time-independent. As part of the RaDyO project, numerous efforts have been focused on measuring the dynamic light field as close as half a meter below the ocean surface. State-of-the-art technologies and instruments have enabled RaDyO researchers to measure different aspects of the dynamic underwater light field, but each instrument has its limitations. A video camera system named RADCAM [*van Dommelen et al.*, 2010] measures the full angular distribution of the unpolarized light field (i.e., the radiance field) at a frame rate of up to 12 Hz, but it does not measure the polarization states; a polarimeter system named DPOL [*Voss et al.*, 2008] measures the full angular distribution of the light field along with the full linear polarization state, but does not reveal the highly

[1]Department of Physics and Astronomy, Texas A&M University, College Station, Texas, USA.
[2]Department of Physics, University of Miami, Coral Gables, Florida, USA.
[3]Department of Oceanography, Dalhousie University, Halifax, Nova Scotia, Canada.
[4]Satlantic Inc, Halifax, Nova Scotia, Canada.
[5]Ocean and Climate Physics Division, Lamont-Doherty Earth Observatory, Columbia University, Palisades, New York, USA.
[6]Department of Computer Science, University of Massachusetts, Amherst, Massachusetts, USA.

0148-0227/11/2011JC007278

dynamic feature of the light field since the measurements are still images; a high-speed radiometer system named PORCUPINE [*Darecki et al.*, 2011] measures the underwater irradiance as well as radiance along several representative directions at a sampling rate of 1 kHz but does not measure the polarization states or the angular distribution. In other words, even with the most advanced instruments, it is not yet possible to measure the full underwater dynamic polarized light field, characterized by the spatial, temporal, and angular distributions along with the full polarization states, in the surface boundary layer.

[4] Using numerical approaches to study the underwater polarized light field became possible after *Chandrasekhar* [1960] introduced radiative transfer theories to analytically describe the propagation of radiation in multiple scattering media such as the ocean and the atmosphere. Various solutions of the radiative transfer equation have been reported since then. Popular radiative transfer models that solve for the polarized light field in the ocean include the invariant imbedding method [*Adams and Kattawar*, 1970; *Mobley*, 1994], the matrix operator method [*Kattawar et al.*, 1973a; *Plass et al.*, 1973], and the Monte Carlo method [see, e.g., *Kattawar et al.*, 1973b; *Kattawar and Adams*, 1989; *Zhai et al.*, 2008a]. Most of these models were originally implemented assuming a plane-parallel geometry in which the medium was homogeneous in the horizontal dimension and the air-sea interface was flat. These assumptions substantially simplified the system and made solutions to the radiative transfer equation practical with limited computational resources. A statistical wave slope model proposed by *Cox and Munk* [1954] has been widely used to account for effects of wind-roughened ocean surfaces on the underwater light field in radiative transfer models [see, e.g., *Plass et al.*, 1975; *Jin et al.*, 2006; *Zhai et al.*, 2010]. Results from these models give the temporal- and spatial-averaged light field when surface waves are present. As shown by *Adams et al.* [2002] and *Tonizzo et al.* [2009], numerical simulations are capable of reproducing the polarized light field from direct measurements, provided that appropriate atmospheric and oceanic optical properties are used as input to the model.

[5] However, all the above studies used a plane parallel one-dimensional (1-D) model and lacked the capability to resolve the horizontal distribution of the light field. Furthermore, they treated the coupled atmosphere-ocean system as a static system and neglected its dynamic nature. On the other hand, the underwater light field, especially that very close to the ocean surface, is highly dynamic primarily due to variations in the transmission of the incident radiance distribution, i.e., the sky light, across the dynamic ocean surface. This dynamic light field is inherently three-dimensional (3-D) as the instantaneous wave slope field imposes inhomogeneity in the horizontal dimension. Very recently attention has been placed on model simulations of the underwater light field in a dynamic ocean. *Hedley* [2008] reported a geometric-optics-based 3-D radiative transfer model that solves for the unpolarized underwater light field. *He et al.* [2010] proposed a polarized model based on the matrix-operator method.

[6] As part of the RaDyO effort, a hybrid polarized radiative transfer model [*Zhai et al.*, 2008a, 2008b] has been developed to make model simulations of the dynamic underwater polarized light field practical. This hybrid model is optimized and highly efficient for simulating temporal variations in the polarized light field under a dynamic ocean surface. It has been used to generate dynamic polarized light fields under hypothetical wave slope fields assuming a certain power spectral density [*You et al.*, 2009]. A fast irradiance version has been used to reproduce the highly dynamic underwater irradiance field, and the model predictions are consistent with measurements made during the RaDyO Santa Barbara Channel experiment [*You et al.*, 2010] at depths ranging from 0.87 m to 2.85 m.

[7] In this paper, we improve the performance of the hybrid model and apply it to simulations of the underwater polarized light field using measured high-resolution wave slope data as input. The simulated underwater radiance field is compared to both DPOL and RADCAM measurements and the simulated polarization states is compared to DPOL measurements acquired during the RaDyO Santa Barbara Channel experiment. Qualitative agreements are observed for both the radiance and polarization states. The paper is organized as follows: in section 2 we review the hybrid radiative transfer model and introduce improvements that make predictions of the high resolution light field possible; in section 3 we describe the wave slope data and the water inherent optical properties measurements that are used as input to the hybrid model simulations; in section 4 we present model predictions of the underwater polarized light field, discuss the capability of the hybrid model in reproducing the dynamic features of the light field, and compare model predictions with field measurements of underwater light fields from the DPOL and RADCAM instruments; conclusions are given in section 5.

2. The Hybrid Radiative Transfer Model

[8] The methodology of the hybrid radiative transfer model has been previously reported [*Zhai et al.*, 2008b; *You et al.*, 2009]. In these studies, the model was used to generate the dynamic polarized underwater light field with relatively low spatial resolution (0.26 m in one dimension and homogeneous in another by *Zhai et al.* [2008b] and 1.4 m by 1.4 m from *You et al.* [2009]) and with limited angular resolution (only 12 viewing zenith angles in the downwelling hemisphere and 15° increment in the azimuth angle in both studies). These resolutions were too coarse to resolve the spatial and angular variations in the real-world dynamic underwater light field. Use of higher resolutions would lead to prohibitively large storage space and much longer computer time for the previous reported hybrid model, and improvements are required. In this section we briefly describe the hybrid model before introducing the improvements.

2.1. Methodology

[9] The hybrid radiative transfer model was specifically designed for simulations of the light field immediately beneath a dynamic ocean surface (within several meters depth), where the instantaneous wave slope field dominates the variability in the light field. This dominance opens up possibilities for the design of the hybrid model. Note that in a dynamic atmosphere-surface-ocean system, usually only the surface layer is highly dynamic with possible temporal variations in the wave slope field much shorter

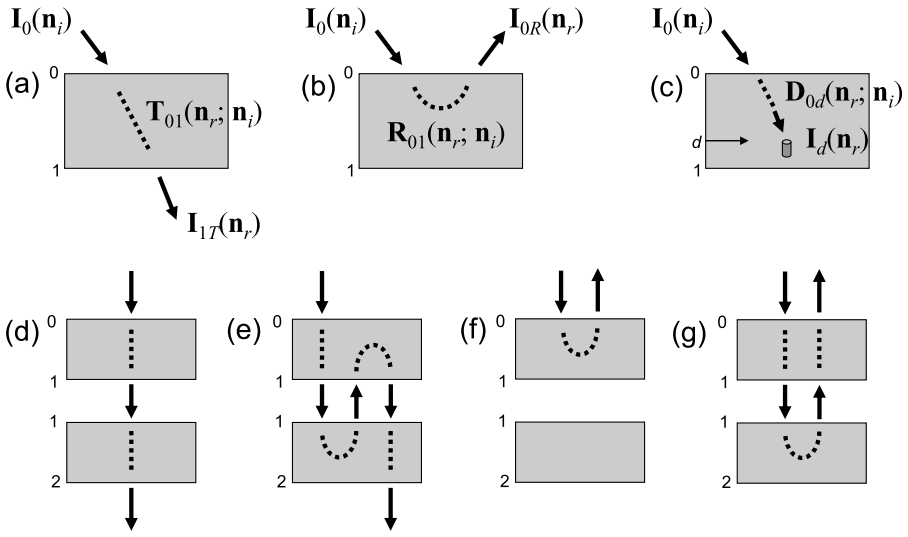

Figure 1. (a–c) Representative impulse-response functions for a single layer; (d–g) coupling of impulse-response functions in a two-layer system.

than a second. On the other hand, the optical properties in the atmosphere and ocean (including the aerosol loading, water absorption and scattering, oceanic volume scattering function, etc.) are slowly varying and can be considered as time-independent within the time frame of interest, for example, seconds to minutes. Therefore, we can treat the atmosphere and ocean as static parts of the system and solve for the radiative transfer in these two parts in advance. These static parts are then coupled to the time-dependent surface layer to give the dynamic light field in the coupled system.

[10] Several methods are available to solve for the radiative transfer equation using coupling techniques, among which we chose the matrix operator method. This method separates a coupled system into several layers. As in any numerical model, the light field in the matrix operator method is discretized. For example, the radiance along some direction in a 1-D light field denoted by $\mathbf{I}(\theta, \phi)$ is actually the light field averaged over a small but finite solid angle, $\mathbf{I}(\theta \pm \Delta\theta, \phi \pm \Delta\phi)$. The radiative transfer in each layer is characterized by *impulse-response functions*, which relate a light field of interest as a *response* to all possible incident light fields, i.e., *impulses*. As an example, for an impulse $\mathbf{I}_0(\theta_i, \phi_i)$ at boundary 0 along any direction (θ_i, ϕ_i), one can have a transmitted response $\mathbf{T}_{01}(\theta_r, \phi_r, \theta_i, \phi_i)\mathbf{I}_0(\theta_i, \phi_i)$ at boundary 1 along any direction (θ_r, ϕ_r) (Figure 1a), where $\mathbf{T}_{01}$ is a *transmission function* and represents the combined effects of the inherent optical properties, the absorption and volume scattering coefficient. The total transmission $\mathbf{I}_{1T}(\theta_r, \phi_r)$ can always be linearly related to all possible impulses $\mathbf{I}_0(\theta_i, \phi_i)$ such that, in a 1-D static scheme,

$$\mathbf{I}_{1T}(\theta_r, \phi_r) = \sum_{\theta_i, \phi_i} \mathbf{T}_{01}(\theta_r, \phi_r; \theta_i, \phi_i)\mathbf{I}_0(\theta_i, \phi_i). \tag{1}$$

[11] Similarly, a *reflection function* $\mathbf{R}_{01}$ relates the reflection by the medium to the same impulse light fields (Figure 1b). As shown in Figure 1c, for a detector within the medium, a *detector response function* $\mathbf{D}_{0d}$ may be defined. These impulse-response functions can be calculated using any radiative transfer model for the single layer. As mentioned before, in numerical implementations the light field is discretized; therefore an impulse-response function is in the form of a multidimensional matrix (four-dimensional in the 1-D scheme), which acts on the impulse light field as an operator to get the response light field. The summation in equation (1) can then be regarded as a four-dimensional matrix multiplying a two-dimensional vector

$$\mathbf{I}_{1T}(\mathbf{n}_r) = \mathbf{T}_{01}(\mathbf{n}_r; \mathbf{n}_i) \cdot \mathbf{I}_0(\mathbf{n}_i), \tag{2}$$

where a notation $\mathbf{n} = (\theta, \phi)$ has been introduced to represent the direction for simplicity.

[12] The impulse-response functions $\mathbf{T}_{01}$, $\mathbf{R}_{01}$ and $\mathbf{D}_{0d}$ characterize the radiative transfer in each individual layer. Multiple layers can be coupled noting that a response for one layer can be an impulse for another. Therefore, the radiative transfer in the coupled multilayer system is as straightforward as matrix multiplication operations. In the simplest two-layer system (Figures 1d–1g), the transmitted light field at boundary 2 ($\mathbf{I}_{2T}(\mathbf{n}_r)$) and the reflected light field at boundary 0 due to the two layers ($\mathbf{I}_{0R}(\mathbf{n}_r)$) can be written as

$$\begin{aligned} \mathbf{I}_{2T}(\mathbf{n}_r) &= \mathbf{T}_{02}(\mathbf{n}_r; \mathbf{n}_i) \cdot \mathbf{I}_0(\mathbf{n}_i), \\ \mathbf{I}_{0R}(\mathbf{n}_r) &= \mathbf{R}_{02}(\mathbf{n}_r; \mathbf{n}_i) \cdot \mathbf{I}_0(\mathbf{n}_i), \end{aligned} \tag{3}$$

where the effective transmission and reflection functions ($\mathbf{T}_{02}$ and $\mathbf{R}_{02}$, respectively) can be written as expansions of coupling terms

$$\begin{aligned} \mathbf{T}_{02} &= \mathbf{T}_{12} \cdot \mathbf{T}_{01} + \mathbf{T}_{12} \cdot \mathbf{R}_{10} \cdot \mathbf{R}_{12} \cdot \mathbf{T}_{01} + \ldots, \\ \mathbf{R}_{02} &= \mathbf{R}_{01} + \mathbf{T}_{10} \cdot \mathbf{R}_{12} \cdot \mathbf{T}_{01} + \ldots \end{aligned} \tag{4}$$

Here only the first two orders of coupling terms are explicitly shown, and summations over intermediate arguments are implied by matrix multiplications. These coupling terms are also illustrated in Figures 1d–1g. In a typical matrix operator calculation, several orders of coupling terms are included until contributions from higher order terms are negligible.

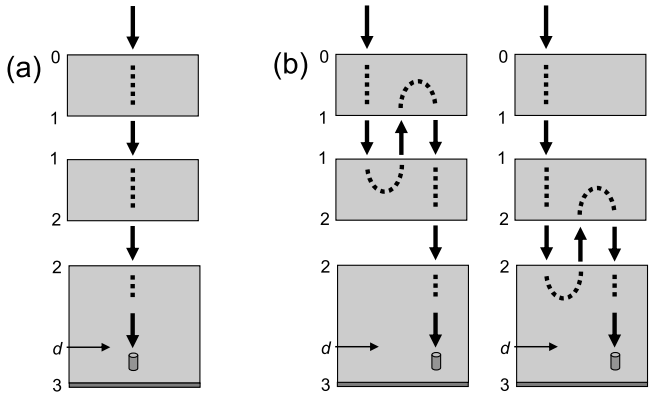

Figure 2. Partition of the coupled atmosphere-ocean system into three parts and the leading orders of coupling terms in the matrix operator method.

[13] In the matrix operator scheme, the coupled atmosphere-ocean system can be conveniently divided into three parts: the atmosphere, the air-sea interface, and the ocean along with its bottom (Figure 2). Following the above coupling scheme, the light field $\mathbf{I}_d$ observed by a detector at depth d below the ocean interface can be written as

$$\mathbf{I}_d = \mathbf{D}_{0d} \cdot \mathbf{I}_0, \tag{5}$$

where the effective detector response function $\mathbf{D}_{0d}$ is given by the following expansion (illustrated in Figure 2):

$$\begin{aligned}\mathbf{D}_{0d} = {} & \mathbf{D}_{2d} \cdot \mathbf{T}_{12} \cdot \mathbf{T}_{01} + \mathbf{D}_{2d} \cdot \mathbf{T}_{12} \cdot \mathbf{R}_{10} \cdot \mathbf{R}_{12} \cdot \mathbf{T}_{01} \\ & + \mathbf{D}_{2\mathrm{d}} \cdot \mathbf{R}_{21} \cdot \mathbf{R}_{23} \cdot \mathbf{T}_{12} \cdot \mathbf{T}_{01} + \ldots,\end{aligned} \tag{6}$$

where labels 0 through 3 denote the top of the atmosphere, the upper and lower surface of the air-sea interface and the bottom of the ocean, respectively.

[14] The above formalism works in the 1-D static situation. In a 3-D dynamic system, the light field and each impulse-response function are a function of five more arguments: the impulse and response positions $\mathbf{r}_i = (x_i, y_i)$ and $\mathbf{r}_r = (x_r, y_r)$, and the time t. For example, $\mathbf{T}_{01}(\mathbf{n}_r; \mathbf{n}_i)$ becomes $\mathbf{T}_{01}(\sigma_r; \sigma_i; t)$, where the notation $\sigma = (\mathbf{n}, \mathbf{r})$ is used, and the effective detector response function (equation (6)) becomes

$$\begin{aligned}\mathbf{D}_{0d}(t) = {} & \mathbf{D}_{2d}(t) \cdot \mathbf{T}_{12}(t) \cdot \mathbf{T}_{01}(t) + \mathbf{D}_{2d}(t) \cdot \mathbf{T}_{12}(t) \cdot \mathbf{R}_{10}(t) \cdot \mathbf{R}_{12}(t) \\ & \cdot \mathbf{T}_{01}(t) + \mathbf{D}_{2d}(t) \cdot \mathbf{R}_{21}(t) \cdot \mathbf{R}_{23}(t) \cdot \mathbf{T}_{12}(t) \cdot \mathbf{T}_{01}(t) + \ldots,\end{aligned} \tag{7}$$

where the σ arguments have been omitted while the t arguments are shown explicitly.

[15] As aforementioned, in the dynamic atmosphere-surface-ocean system, only the surface layer needs to be treated dynamically. On the other hand, the atmospheric and oceanic impulse-response functions are almost static and can be pre-calculated using, for example, a Monte Carlo model. The three parts are then coupled to give the dynamic detector response function $\mathbf{D}_{0d}(t)$ in equation (7), which now becomes

$$\begin{aligned}\mathbf{D}_{0d}(t) = {} & \mathbf{D}_{2d} \cdot \mathbf{T}_{12}(t) \cdot \mathbf{T}_{01} + \mathbf{D}_{2d} \cdot \mathbf{T}_{12}(t) \cdot \mathbf{R}_{10} \cdot \mathbf{R}_{12}(t) \cdot \mathbf{T}_{01} \\ & + \mathbf{D}_{2d} \cdot \mathbf{R}_{21}(t) \cdot \mathbf{R}_{23} \cdot \mathbf{T}_{12}(t) \cdot \mathbf{T}_{01} + \ldots\end{aligned} \tag{8}$$

[16] The dynamic underwater light field $\mathbf{I}_d(t)$ is then related to any incident light field as

$$\mathbf{I}_d(t) = \mathbf{D}_{0d}(t) \cdot \mathbf{I}_0, \tag{9}$$

where $\mathbf{I}_0$ is the incident solar flux or impulse, and can also be treated statically in cases of interest.

[17] As shown by *You et al.* [2009], relevant coupling terms in equation (8) can be re-organized such that

$$\mathbf{D}_{0d}(t) = \left(\mathbf{D}_{2d}^{(0)} + \mathbf{D}_{2d}^{\mathrm{diff}}\right) \cdot (1 + \mathbf{R}_{21}(t) \cdot \mathbf{R}_{23}) \cdot \mathbf{T}_{12}(t) \cdot \mathbf{T}_{01,\mathrm{eff}}, \tag{10}$$

where the in-water detector response function $\mathbf{D}_{2d}$ is separated into a direct part $\mathbf{D}_{2d}^{(0)}$ that corresponds to the exponential extinction of the incident light beam in the ocean and a diffuse part $\mathbf{D}_{2d}^{\mathrm{diff}}$ due to multiple scattering in the ocean. In equation (10), the impulse-response functions $\mathbf{D}_{2d}^{\mathrm{diff}}$, $\mathbf{R}_{23}$ and $\mathbf{T}_{01,\mathrm{eff}}$ have to be calculated using the 3-D Monte Carlo model, with the relevant horizontal and angular arguments being one of the discretized grid points. On the other hand, the surface impulse-response functions $\mathbf{R}_{21}(t)$ and $\mathbf{T}_{12}(t)$ are determined by Fresnel formulas; their angular arguments can be any value but are binned into one of the grid points. Furthermore, it is helpful to use separate spatial discretizations such that the atmosphere and ocean are in coarser *medium grids* and the surface is in finer *surface grids*. The in-water-direct detector response function $\mathbf{D}_{2d}^{(0)}$ does not relate light fields in different directions and is just a product of delta functions

$$\mathbf{D}_{2d}^{(0)}(\mathbf{r}_d, \mathbf{n}_d; \mathbf{r}_2, \mathbf{n}_2) = e^{-\tau} \widetilde{\delta}(\mathbf{r}_d, \mathbf{r}_2) \delta(\mathbf{n}_d, \mathbf{n}_2), \tag{11}$$

where $e^{-\tau}$ is the extinction, the angular part is just a two-dimensional Kronecker delta function $\delta(\mathbf{n}_r, \mathbf{n}_i)$

$$\delta(\mathbf{n}_r, \mathbf{n}_i) = \begin{cases} 1, & (\mathbf{n}_r = \mathbf{n}_i) \\ 0, & (\mathbf{n}_r \neq \mathbf{n}_i), \end{cases} \tag{12}$$

and the horizontal part is written as a modified Kronecker delta function such that

$$\widetilde{\delta}(\mathbf{r}_r, \mathbf{r}_i) = \begin{cases} 1, & (\mathbf{r}_r \text{ and } \mathbf{r}_i + \Delta\mathbf{r} \text{ are in the same medium grid}) \\ 0, & (\text{otherwise}). \end{cases} \tag{13}$$

Here $\Delta\mathbf{r} = (\cos\theta \cos\phi, \cos\theta \sin\phi)d$ is determined by a backward ray tracing technique that traces the photon from the detector to the sea surface along its direction of propagation. As implied by equation (13), the underwater light field represented by $\mathbf{I}_d(\mathbf{r}, \mathbf{n}, t)$ in equation (9) is spatially averaged over a medium grid and has a rather coarse spatial resolution.

2.2. A High-Resolution Algorithm

[18] In the hybrid model introduced in section 2.1, the angular and spatial resolutions of the simulated light field are the same as that of the impulse-response functions. Therefore, the storage space becomes an issue when high angular and/or spatial resolutions are desired. It is possible to improve the spatial resolution noting that the in-water-direct detector response function $\mathbf{D}_{2d}^{(0)}$ (equation (11)) involved a spatial average over the medium grid (see the definition

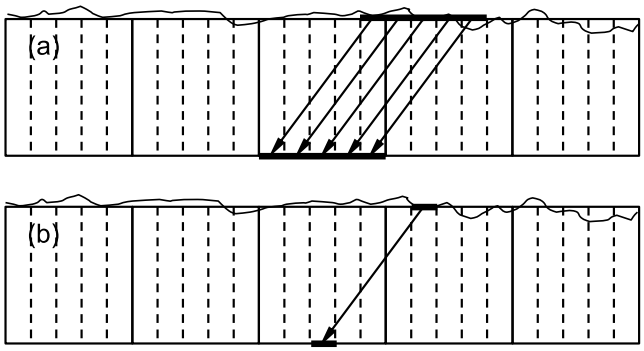

Figure 3. One-dimensional illustrations of the (a) spatial-averaged and (b) non-spatial-averaged schemes involved in the coupling of the in-water-direct response function. The atmosphere and ocean are discretized into medium grids (solid lines), while the surface is discretized into finer surface grids (dashed lines). Solid bars denote the surface grids to be included in the determination of the response function.

of $\tilde{\delta}(\mathbf{r}_r, \mathbf{r}_i)$ in equation (13) and Figure 3a), which leads to a spatial resolution the size of the medium grid. To obtain a higher spatial resolution in this part, the spatial average can be omitted such that equation (13) becomes

$$\tilde{\delta}'(\mathbf{r}_r, \mathbf{r}_i) = \begin{cases} 1, & (\mathbf{r}_r = \mathbf{r}_i + \Delta\mathbf{r}) \\ 0, & (\text{otherwise}). \end{cases} \tag{14}$$

In the backward ray-tracing algorithm, this can be realized by only tracing light beams from the surface grid at the center of the nominated detector medium grid (Figure 3b). This makes the spatial resolution of the in-water-direct part the same as the size of a surface grid.

[19] Furthermore, the angular resolution in this part can be improved noting that the directions $\mathbf{n}_2$ and $\mathbf{n}_d$ in $\mathbf{D}_{2d}^{(0)}$ do not have to be one of the angular grid points in the Monte Carlo calculations. Therefore, one can actually specify any direction $\mathbf{n}$ in the coupling of this term to other impulse-response functions. On the other hand, the contributions from terms involving $\mathbf{D}_{2d}^{\text{diff}}$ can only be resolved with the angular resolution determined by the angular grids.

[20] At near-surface depths, the main effects of the wind-roughened surface on the angular distribution of the underwater light field are to shift the position of the forward peak and to alter the edge of the Snell's window. The directions close to the forward peak exhibit very high radiances, resulting in a scene dynamic range of more than 10^6. The most obvious feature is then the distorted edge of the Snell's window, which is often characterized by fine structures that can only be resolved with a high angular resolution. In shallow and clear waters, the optical depth is relatively small, so the distortion of the Snell's window is mainly determined by the contribution from coupling terms involving $\mathbf{D}_{2d}^{(0)}$ in equation (10). Under this condition, the high-resolution light field given by the $\mathbf{D}_{2d}^{(0)}$ terms should be the major contribution to the total underwater light field.

[21] We note that the hybrid model only considers the light field due to the solar radiation, absorption and elastic scattering. Contributions from internal sources such as Raman scattering [*Bartlett et al.*, 1998] and chlorophyll fluorescence are ignored. This is reasonable since just below the ocean surface Raman scattering is negligible, and we will be showing results at the wavelength of 532 nm, where contributions from chlorophyll fluorescence are almost non-existent. HydroLight [*Mobley and Sundman*, 2000] calculations show that for case 1 waters and the given detector depths, Raman and chlorophyll fluorescence components are less than 1% of the solar radiation (results not shown).

[22] Furthermore, the model only takes wave slopes into consideration and does not include effects from wave elevations (for example, the shadowing effect). This may introduce substantial errors in the simulated underwater light field just below the ocean surface when quantitative comparisons are desired (i.e., if we use field measurements of the wavefield as model input and compare the model simulated light field with collocated measurements of the light field). But for qualitative comparisons as what we will be discussing in this study, errors caused by neglecting wave elevations are not important. We are working on incorporating wave elevations into the hybrid model, and simulated light field calculated from future models under a measured wavy surface patch will be compared with its counterpart from collocated measurements in future studies.

3. Field Data Used as Input to the Model

[23] In our atmosphere-ocean model, the atmosphere consists of two layers: the top layer is atmospheric molecules and the bottom layer is aerosols. Both layers are conservative, with a single scattering albedo of unity. The ocean is assumed to be homogeneous and has two optically active components mixed together: (1) water molecules and (2) particulates and CDOM. The molecular scattering in both atmosphere and ocean is governed by the Rayleigh scattering phase function and phase matrix. The aerosol scattering is determined by an oceanic aerosol model [*Lenoble and Broquez*, 1984].

[24] In order to generate realistic underwater light fields, some relevant atmospheric and oceanic optical properties are required as input to the hybrid model. Some of them are given by experimental results in the literature. The optical thickness of the atmospheric molecular layer is determined by the equation of *Hansen and Travis* [1974], while the aerosol optical thickness is given by measurements. The scattering and absorption coefficients of seawater molecules (b_w and a_w) are given by measurements from *Smith and Baker* [1981] and from *Pope and Fry* [1997], respectively. Other optical properties are acquired during the RaDyO Santa Barbara Channel field experiment as detailed in sections 3.1 and 3.2.

3.1. Inherent Optical Properties and Volume Scattering Function

[25] The particulate scattering coefficient (b_p) and particulate and CDOM absorption coefficient (a_{pg}) are from field measurements performed in the RaDyO Santa Barbara Channel experiment [*Chang et al.*, 2010]. Since we are most interested in the dynamic features of the underwater light field, we focus on a single wavelength of 532 nm in this study. For each component, the absorption and scattering data are converted into the extinction coefficient ($c = a + b$) and the single scattering albedo ($\omega = b/c$), which are used in

Table 1. Ocean Inherent Optical Properties Used in the Model Simulations

Property	Value
λ (nm)	532
c_w (m^{-1})	0.0460
ω_w	0.0457
c_{pg} (m^{-1})	0.6522
ω_{pg}	0.9314

the model simulations. The extinction and single scattering albedo for both components are listed in Table 1. As seen in the table, at this wavelength the oceanic scattering is dominated by the particulate and CDOM component.

[26] Note that the values for a_{pg} and b_p are averaged values. Temporal and spatial variations in these quantities have been discussed by *Chang et al.* [2010]. However, averaged values are good enough for the purposes of this study.

[27] The volume scattering function (VSF) for particulate scattering is also required. Field measurements of the VSF were made during the RaDyO Santa Barbara Channel experiment. However, the VSF data were not well calibrated at the time of this modeling study. Therefore, we used a *Fournier and Forand* [1994] phase function whose backscatter factor (b_{bp}/b_p) was 0.0049 as given by field measurements. This value is consistent with that calculated from preliminary VSF data. In a dynamic situation, the underwater light field just below the surface is primarily determined by the wave slope field, and the VSF only plays a secondary role. Test runs have shown that there are no significant changes when the particulate VSF changes from a Fournier-Forand to the field measurement, as long as the backscatter factor is the same. Other elements of the particulate Mueller matrix are determined by a reduced Rayleigh phase matrix (see, e.g., *van de Hulst* [1981, p. 81] or *Adams et al.* [2002]) with a depolarization ratio of 0.1. This reduced phase matrix is generally in-line with underwater Mueller matrices measured by *Voss and Fry* [1984] but with less polarization in the forward directions (smaller values for P_{22}/P_{11}, P_{34}/P_{11} and P_{44}/P_{11} elements). This phase matrix applies well to case 1 waters in the Santa Barbara Channel.

3.2. Wave Slopes

[28] *You et al.* [2009] used a hypothetical wave slope field generated from a measured power spectral density. In this study, we were able to use high-resolution wave slope data measured in the Santa Barbara Channel. A shape-from-polarimetry technique [*Zappa et al.*, 2008] was used to derive the two wave slope components ($S_x = \partial z(x, y)/\partial x$ and $S_y = \partial z(x, y)/\partial y$, where $z(x, y)$ is the wave elevation) from instantaneous images of the wavy surface. Each wave slope data set is a 10-min time series of wave slope components at a frame rate of 60 Hz. Each frame covers a surface patch of about 1 m by 1 m, with a spatial resolution of about 1.3 mm by 1.7 mm, which is fine enough to resolve most gravity and gravity-capillary waves that play an important role in determining the dynamic underwater light field. The nominal integration time for each frame is 0.5 to 5 ms. In this study, we used two wave slope data sets measured when the surface wind speed was about 5.1 m s^{-1} (17 September 2008 at 14:13 UTC) and 9.3 m s^{-1} (19 September 2008 at 18:10 UTC), which represent a low-sea and a high-sea situation, respectively. The measured wave slope components S_x and S_y can be used to reconstruct the wave elevation field using a Fourier transform approach based on

$$z(x,y) = \mathcal{F}^{-1}\left[-i\frac{k_x \cdot \mathcal{F}[S_x(x,y)] + k_y \cdot \mathcal{F}[S_y(x,y)]}{k_x \cdot k_x + k_y \cdot k_y}\right], \quad (15)$$

where $\mathcal{F}$ is a Fourier transform, $\mathcal{F}^{-1}$ is an inverse Fourier transform, and k_x and k_y are x and y components of the wave vector.

[29] Figure 4 shows the first frame of a time series of reconstructed wave elevation fields based on the two wave slope data sets. A 2-s time series is available online for each sea condition (Animations 1 and 2). The low-sea situation shows a wavefield that has capillary waves riding on large scale gravity waves, while the high-sea situation wavefield shows both long and short gravity waves as well as capillary waves.

4. Simulation Results

[30] In this section we describe the system setup that was used in our simulations, and then show the underwater polarized light field from model simulations in various cases.

4.1. System Setup

[31] In the simulations, the radiative transfer in the static atmosphere and ocean parts were calculated separately as an independent system. The optical properties of these parts are as described in section 3. The depth of the ocean was assumed to be 10 m with a completely absorptive bottom. The modeled ocean is relatively shallow, and the simulated downwelling radiance would be slightly underestimated as a result of the lack of upwelled photons from the water column below 10 m. However, its effects on the dynamic

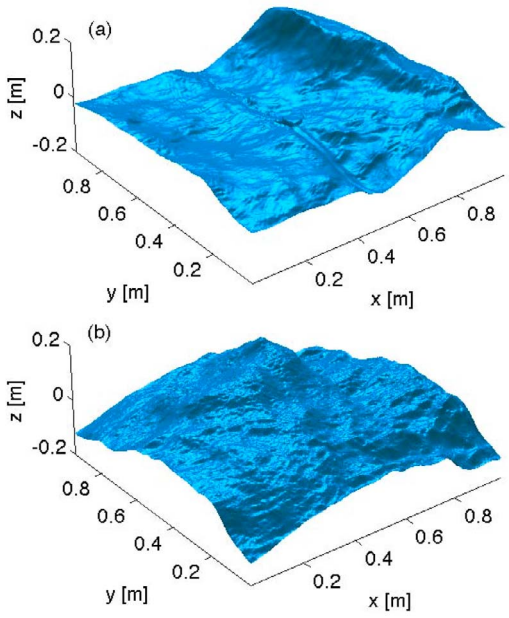

Figure 4. Snapshots from the reconstructed wave elevation fields in (a) the low-sea situation with a surface wind speed of 5.1 m s^{-1} and (b) the high-sea situation with a surface wind speed of 9.3 m s^{-1}.

features are marginal. To get meaningful results at a relatively large detector depth, it is required that the footprint of the Snell's cone on the ocean surface as seen by the detector is confined within the computational domain. For a detector depth of 1 m, the radius of the footprint is about 1.12 m. With this being considered, the 1 m × 1 m area covered by the wave slope data was not sufficient for model simulations. We had to extend it periodically to fill a 3 m × 3 m computational domain. This treatment may introduce some artifacts due to the periodicity in the wave slope field. However, it is unnecessary once wave slope data covering a larger surface area become available.

[32] As mentioned in section 2.2, the spatial resolution of the simulated light field was the same as that of the wave slope data, i.e., 1.3 mm × 1.7 mm. The angular resolution specified in the simulations was 1° in the zenith and 2° in the azimuth angles.

[33] Like any polarized radiative transfer model, the hybrid model uses the Stokes vector notation $\mathbf{I} = [I, Q, U, V]^T$ [see, e.g., *van de Hulst*, 1981] to describe the polarized light field. Interesting quantities include the radiance I, the degree of linear polarization (DoP)

$$\mathrm{DoP} = \sqrt{Q^2 + U^2}/I, \tag{16}$$

and the plane of linear polarization (PoP) that characterizes the orientation of the electric field vector (e-vector) and is described by an angle χ determined by

$$\tan(2\chi) = U/Q, \tag{17}$$

where χ varies from −90° to 90°. It is 0° when the e-vector is in the meridian plane and ±90° when the e-vector is in the horizontal plane.

4.2. Results

[34] The first case we present is the downwelling dynamic polarized light field at 0.2 m under the low-sea wave slope fields (surface wind speed 5.1 m s^{-1}). The Sun was positioned in the x-z plane (see Figure 4) with an azimuth angle $\phi = 0°$. The solar zenith angle was assumed to be 30°. The depth of 0.2 m can be regarded as a nominal averaged depth since wave elevations is not incorporated in the hybrid model. For the wave slope data used in this study, the derived wave elevation never exceeds ±0.2 m (Figure 4), so a nominal depth of 0.2 m makes sure that the detector is always below the air-sea interface even if wave elevations are to be considered.

[35] Figures 5a–5c show three consecutive frames from the simulated dynamic radiance field as seen by a 1.3 mm × 1.7 mm rectangular detector at the center of the computational domain. The units are W m^{-2} nm^{-1} sr^{-1}. The frames are 1/60 s apart from each other. The angular distribution of the downwelling light field, as if one looks into the upper hemisphere, was mapped to a circle such that the center of the circle corresponds to the zenith, the perimeter of the circle corresponds to the horizon, and the $+x$ and $+y$ directions (see Figure 4) point to the right and the bottom of the circle, respectively. The principal plane is horizontal in the plots, with the visual Sun direction to the left of the circle. This can be easily realized by looking at the high radiance area, which is due to the forward-scattered direct Sun light. As a reference, the edge of the Snell's cone in a flat surface case is also shown (dashed circle). We note that the color bar in Figure 5 and radiance Figures 7a, 8a, 9, 10a, 10d, and 11 is chosen to run from 0 to 0.4 W m^{-2} nm^{-1} sr^{-1} such that low radiance levels are visible. However, an artificial over-exposed region is introduced as shown by a white region in Figure 5. This does not mean the simulated or the measured radiance is over-exposed. For clarity, such regions are referred to as "high radiance" areas rather than over-exposed areas.

[36] It is obvious from these snapshots that the edge of the Snell's cone (whose footprint at the surface has a radius of 0.225 m) is highly distorted by the wavy surface. Note that at 0.2 m, a viewing angle of 1° corresponds to a horizontal distance of about 5 mm at the surface. This distance is on the same order of the spatial resolution of the wave slope data. With an angular resolution of 1° × 2°, the simulations were able to resolve the fine distortions in the light field caused by most surface waves. Comparisons across consecutive frames reveal that, within 1/60 s there are noticeable changes in the simulated radiance field, especially around the edge of the Snell's cone. On the other hand, the radiance outside the Snell's cone comes from either in-water scattering or reflection off of the lower surface of the air-sea interface. The former has little dependence on the instantaneous wavefield; the latter is highly dependent on the wavefield but is much lower than the transmitted skylight. Therefore, the light field outside the Snell's cone shows few temporal changes.

[37] A 2-s animation showing the time series of the simulated dynamic radiance field is available online (Animation 3). Animation 3 is slowed down by three times to a 20 Hz frame rate to facilitate visualization of temporal variations. The time series shows realistic temporal variations that are qualitatively comparable to field measurements. First, the overall shape of the Snell's cone changes as a result of the variation in the larger scale pattern (primarily due to longer gravity waves) of the wave slope field. These gravity waves also cause movement and distortion of the high radiance region, which corresponds to the forward-scattered light. Second, there are much faster changes in the fine structures around the edge of the Snell's cone, which are due to the variations of smaller scale wave structures, i.e., capillary waves that ride on gravity waves. Also caused by the short waves are some wave-like features around the high radiance region. These features are probably due to wave focusing from local wave slopes. Third, some temporal variations in the relatively dark radiance field outside the Snell's cone become noticeable in Animation 3. As mentioned above, these are due to the reflection of in-water upwelling radiance by the lower surface of the dynamic air-sea interface.

[38] For comparison, Figure 5d shows the simulated angular distribution of the light field shown in Figure 5a, but using the previously reported algorithm, i.e., with much lower spatial and angular resolutions. It is obvious that simulations using the lower resolutions resulted in a poor representation of the fine structures in the light field, although they were successful in reproducing the overall shape of the distorted Snell's cone.

[39] Figures 6a and 6b show patterns of the DoP and PoP (angle χ), respectively, that correspond to the instantaneous

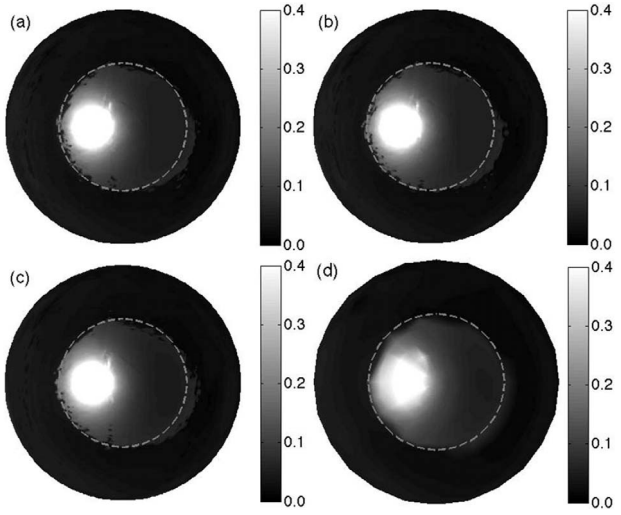

Figure 5. Simulated underwater downwelling radiance field in units of W m^{-2} nm^{-1} sr^{-1} at 0.2 m beneath the low-sea wave slope field. The wavelength is 532 nm. (a–c) Three consecutive frames 1/60 s apart from each other. (d) Same as Figure 5a except for the radiance field as if the low-resolution algorithm were used. See text for the mapping from the downwelling hemisphere to a circle. The Snell's cone in a flat-surface case is marked (dashed circle) for reference.

light field shown in Figure 5a. In both patterns, the overall shape of the distorted Snell's cone and the fine structures around its edge are the same as that seen in the radiance pattern (Figure 5a). The fine structures are obvious in the DoP pattern, where there is a big discontinuity between the more polarized inside region (DoP ~ 0.6, cyan region) and the less polarized outside region (DoP ~ 0.2, orange region) in the anti-solar half plane. The Snell's cone edge close to the high radiance region disappears as both sides of the cone have almost no polarization (DoP < 0.1, red region). The edge of the Snell's cone is not as obvious in the PoP pattern, where the inside region has PoP around ±60° (orange or violet regions) while the outside region has PoP close to ±90° (red or deep violet regions). The χ angle outside the Snell's cone is always close to ±90° since the e-vector orientation is almost perpendicular to the meridian plane. Note that –90° and +90° actually represent the same plane of polarization, and the discontinuity is introduced by the definition of the angle.

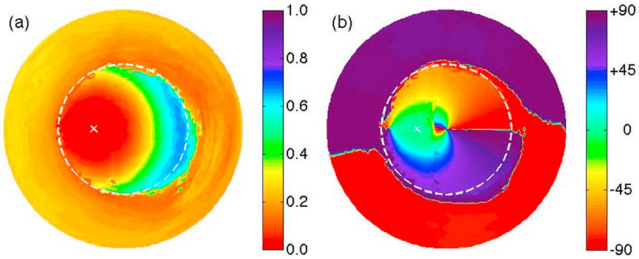

Figure 6. Same as Figure 5a except for the (a) DoP and (b) PoP patterns. The white cross marks the average refracted location of the Sun.

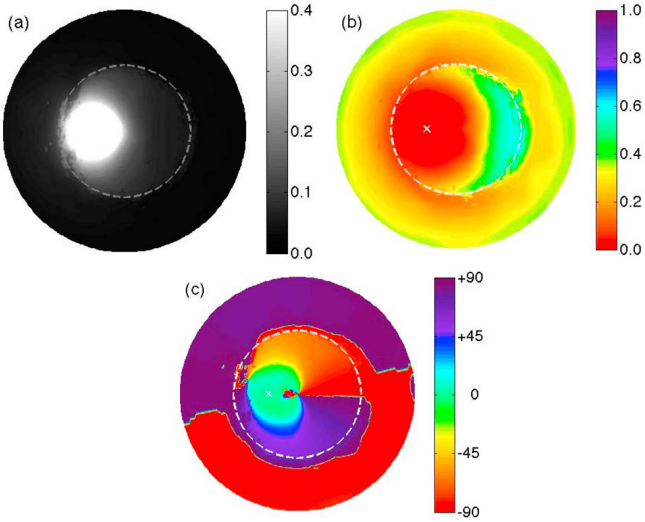

Figure 7. Same as Figures 5a and 6 except for the polarized light field at 1 m below the low-sea ocean surface: (a) radiance (in units of W m^{-2} nm^{-1} sr^{-1}); (b) DoP; and (c) PoP.

[40] Two-second animations showing the dynamic DoP and PoP patterns are available online (Animations 4 and 5). In the DoP time series, there are noticeable temporal variations both inside and outside the Snell's cone. Inside the Snell's cone, the unpolarized region moves and changes shape due to longer waves passing by; outside the Snell's cone, although the level of DoP is always in the 0.1 to 0.3 range, numerous wave-like features can be seen, which are probably due to reflections involving short waves. In the PoP time series, there are less temporal variations inside the Snell's cone, but much more action outside the Snell's cone due to the artificial discontinuity between –90° and +90°. Note that the light field outside the Snell's cone is due either to internal reflection off the lower surface of the air-sea interface or in-water scattering. The simulation results imply that, although this region exhibits relatively low radiance, the corresponding degree and plane of polarization are highly sensitive to the overhead wave slope fields and move extremely fast.

[41] We did the same simulations for a detector at a greater depth, 1 m below the ocean surface. Figure 7 shows the first frame of simulated radiance, DoP, and PoP time series at this depth. Comparing simulated radiance fields at the two depths (Figures 5 and 7a), the light field outside the Snell's cone at 1 m is generally brighter due to the stronger scattered light from both single and multiple scattering that is accumulated over the depth. This also makes the edge of the Snell's cone not as sharp as it was at 0.2 m. The overall downwelling light field inside the Snell's cone is less polarized (Figures 6a and 7b) as in-water scattering tends to depolarize the light field that was previously polarized either by transmitting through or reflecting off of the air-sea interface. On the other hand, the light field outside the Snell's cone becomes more polarized. There is not an obvious change in the plane of polarization (Figures 6b and 7c). As for dynamic features, first, the overall shape of the Snell's cone at 1 m suffers less distortion as its footprint on the surface has a much larger radius of 1.125 m and a larger patch of the wavy surface comes into play in determining the shape of

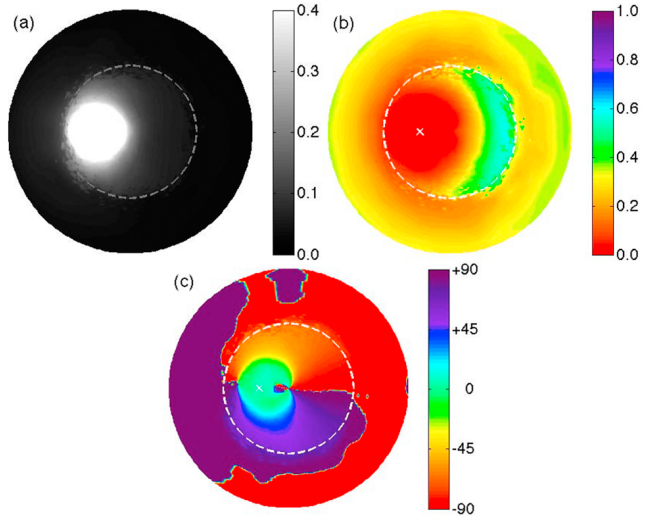

Figure 8. Same as Figure 7 except for results at 1 m below the high-sea surface.

the Snell's cone. Note that the footprint of the Snell's cone is now larger than the 1 m × 1 m wave patch covered by the real wave slope data set. However, no artifact due to the imposed periodic boundary condition can be seen in the simulated light fields. Second, the structures introduced by the shorter capillary waves become even finer since the detector is further away from the wavy surface and the viewing solid angle corresponding to the same wave components decreases.

[42] Accompanying animations showing 2-s time series are available online as well (Animations 6, 7, and 8). The overall shape of the Snell's cone and the patterns inside it do not move as much as at 0.2 m, since a larger surface area comes into play to distort these patterns. Similar to the 0.2 m case, variability outside the Snell's cone is almost negligible in the radiance time series but substantial in the DoP and PoP time series. The wave-like features in the 0.2 m DoP time series are now strongly suppressed since the surface reflected light, which is highly sensitive to short scale wave components, has to undergo more scattering events before reaching the detector.

[43] The next case we simulated was when the detector was 1 m below the high-sea wave slopes (Figure 4b), which corresponds to a surface wind speed of 9.3 m s^{-1} and shows much more small-scale wave components comparing to the low-sea wave slopes (Figure 4a). The resulting radiance, DoP and PoP patterns are shown in Figure 8. In this case, we expect to see even finer structures in the angular distribution of the underwater light field. However, note that a 1° viewing angle at this depth corresponds to a surface distance of about 2.5 cm at the edge of the Snell's cone. Therefore, the angular resolution we use is not sufficient to resolve the shortest wave components that are in the model, especially in the high-sea situation. As seen in Figure 8, although the model did resolve even fine structures compared with Figure 7, it reaches its limitation when using an angular resolution of 1° × 2°. An interesting point to notice is that, in simulations based on the statistical Cox-Munk wave slope model, increasing the surface wind speed will result in an increased blurriness at the edge of the Snell's cone. In simulations using instantaneous wave slope data, however, the sharpness of the Snell's cone edge does not depend on the surface wind speed. One would expect the increased blurriness to occur after many instantaneous light fields are averaged to give a temporal-averaged light field [see, e.g., *You et al.*, 2009, Figure 5]. In the simulated time series (available in the auxiliary material, Animations 9, 10 and 11), the temporal variations under the high-sea wave slopes seem to be similar to those under the low-sea wave slopes.[1]

[44] All results shown above were based on the original wave slope data with a sampling rate of 60 Hz and a nominal integration time of 0.5 to 5 ms for each frame. On the other hand, the integration time used in underwater light field measurements can be much longer due to extremely low signals available at depth. For example, in the upwelling light field measurements using a polarimeter, the integration time can be as long as 0.1 s. As shown above, the angular distribution of the light field may have changed substantially over this duration. To investigate the effect of the integration time to the measured dynamic light field, we averaged the simulated 60 Hz light fields over 0.1 s, or 6 frames, to take into account the much longer integration time used in light field measurements. Figure 9 shows the time-integrated light field at 0.2 m below the low-sea wave slopes. The simulated time series is available online as well (Animation 12). Comparing these results to those shown in Figure 5 and Animation 3, it is obvious that by doing the temporal average over 0.1 s, we lose some features in the angular distribution of the light field that are beyond this temporal resolution, even if the angular resolution remains unchanged. Most of the fine structure around the edge of the Snell's cone is also smoothed out by the temporal integration. It should be noted that the integration time of a wave slope measurement is generally much shorter than that of an underwater light field measurement since the available ambient light is always stronger above the surface. Obviously then, model simulations can generate underwater light fields that contain more dynamic information than direct measurements, as long as the required input parameters, especially high-resolution wave slope data, are available.

4.3. Comparison With Measured Underwater Light Fields

[45] An important aspect of this study is to investigate if the model-simulated underwater dynamic light field is consistent with that from direct measurements assuming the same temporal, spatial and angular resolutions. In this section we show comparisons of model simulations to field measurements of the underwater polarized light field. The measured light fields that we are comparing with were acquired during the RaDyO Santa Barbara Channel experiment using two instruments.

[46] First we compare model simulations with polarized light field measured by DPOL [*Voss et al.*, 2008] on 18 September 2008, at a detector depth of 1 m and a wavelength of 520 nm. The DPOL instrument takes still images of the polarized radiance distribution at integration

[1] Auxiliary materials are available in the HTML. doi:10.1029/2011JC007278.

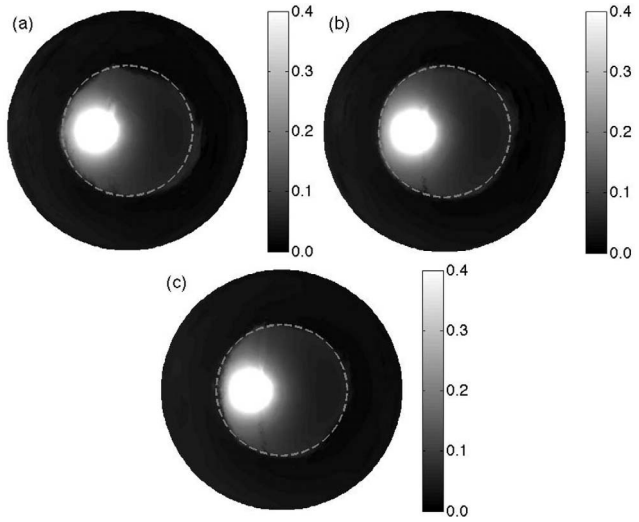

Figure 9. Same as Figure 5 except for the simulated radiance field assuming an integration time of 0.1 s. The finest structures are lost in this case.

times between 30 and 3 ms. Each still image contains the polarization information to calculate the complete Stokes vector. However, with time required for data storage and changing the spectral filter, one frame can be collected every 17 s. The CCD array in DPOL has dimensions 1600 × 1200 pixels, however this is split into 4 quadrants (one for each polarization signal), and with averaging, the final resolution of the DPOL system is approximately one degree at the center of the image. Since DPOL uses fisheye lenses, the resolution is a function of zenith angle from the center, increasing linearly with zenith angle [*Miyamoto*, 1964]. The latitude and longitude of the measurement were 34.20°N and 119.63°W, respectively. The sky was very clear; the surface wind speed was about 10 knots or 5 m s^{-1} and the surface condition was "very small wave with small ripples." These environmental conditions were generally in-line with the previously discussed low-sea situations (wind speed of 5.1 m s^{-1}). During this light field measurement, the solar zenith angle was 54°. The exposure time of this measurement was 0.01 s.

[47] Shown in Figures 10a–10c are measured angular distributions of the downwelling radiance, DoP, and PoP, respectively. Due to tilt of the instrument, the measured light field did not cover the whole downwelling hemisphere, whose boundary is denoted by a black circle. To be consistent with Figures 5 to 9, the distributions are rotated such that the principal plane is horizontal with the solar-half to the left. Here the edge of the Snell's cone is distorted by the wavy surface. In the radiance images there are several areas where there are obvious internal reflections in the instrument caused by the shallow measurement depth and the direct solar radiance level (radiance up to 7 orders of magnitude greater than other areas in the image). These areas are outlined with the white lines in the radiance image, and were cut out of the Q/I and U/I data files. Linear interpolation was done across these areas in the Q/I and U/I images, and with these revised data files the DoP and PoP were calculated. In all the measured data fields there are also obviously influences of the measurement platform (R/P Flip) and the booms extending from this platform. In the DoP and PoP patterns, there are lots of noise-like structures throughout the whole field of view, probably due to both the wavy surface and platform perturbations. Figures 10d–10f show the corresponding angular distributions from model simulations with a solar zenith angle of 55°, a surface wind speed of 5.1 m s^{-1}, and a detector depth of 1 m.

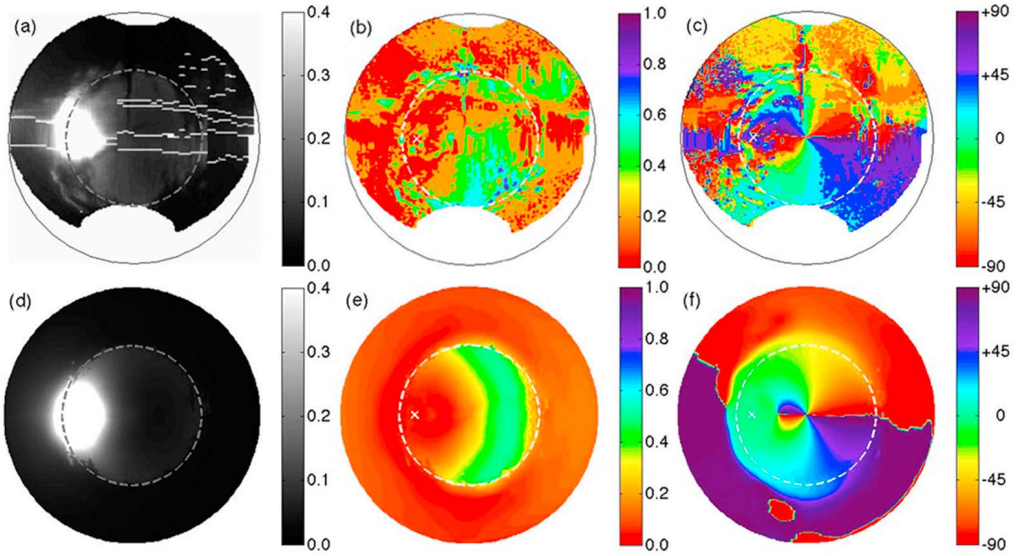

Figure 10. Comparison of (a–c) DPOL-measured and (d–f) model-simulated downwelling polarized light field at 1 m below a wavy ocean surface when the surface wind speed is about 5 m s^{-1}. Figures 10a and 10d show the radiance in units of W m^{-2} nm^{-1} sr^{-1}; Figures 10b and 10e show the degree of polarization; Figures 10c and 10f show the plane of polarization. In the measured radiance image (Figure 10a) there are areas which have been affected by the inner reflections of the system from the direct sunlight. These areas have been addressed as discussed in the text.

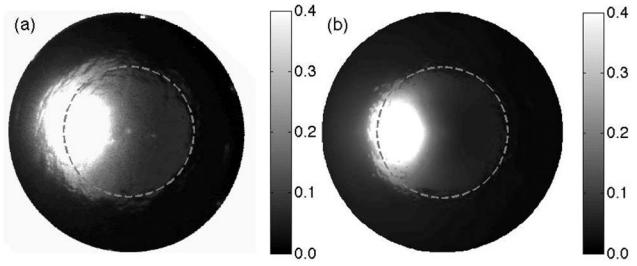

Figure 11. Comparison of downwelling radiance field at 1 m (a) measured by RADCAM and (b) simulated by the hybrid model in units of W m^{-2} nm^{-1} sr^{-1}. The solar zenith angle is 45°, and the surface wind speed is about 10 m s^{-1}.

[48] Note that the wave slope data used in the model simulation were not synchronized to or collocated with the light field measurements, although the two measured data sets share the same surface wind speed and the wave slope data are believed to be similar to that above the measured light field. The simulated light field based on these wave slope data should therefore be qualitatively compared to the measured light field. First, the magnitude of the simulated radiance is consistent with the measured data. Second, the edge of the Snell's cone is basically a circle and not as distorted as that seen in the measurement. For the DoP, the patterns inside the Snell's cone are qualitatively consistent with a maximum value around 0.6 in both plots. Outside of the Snell's cone, the measured DoLP varies in between 0.2 to 0.25 in the major part of the field of view, but can be up to 0.4 in a small area; the simulation is at around 0.2 with much less variations. Test runs showed that the simulated polarization outside of the Snell's cone will be higher (~0.4) should we use the Voss and Fry Mueller matrix. The overall pattern in the PoP, especially that in the Snell's cone is consistent as well. Outside the Snell's cone, the measured PoP varies substantially, while the simulated one is very close to ±90°. In both DoP and PoP, the simulations look much less noisy compared with the measurements; the edge of the Snell's cone is almost not recognizable in the measurements while it is in the simulations; also the fine structures at the edge of the Snell's cone are hard to identify in the measurements due to excessive noise. Moreover, the symmetry with respect to the principal plane is well kept in the simulations, but is substantially destructed in the measurements. The discrepancies could come from the difference in the wave slopes used in the simulations and those above the measured light field, although the wind speed was very close in the two cases. Ideally, one should be comparing model simulated light fields using wave slope data that are collocated with and synchronized to the light field measurement. Such combinations of data sets are not yet available. Another possible source of the disagreement is the absence of wave elevations in the hybrid model, which is expected to introduce more distortions.

[49] Simulated underwater radiances (unpolarized light field) were also compared with its counterpart measured by RADCAM [*van Dommelen et al.*, 2010] on 17 September 2008 at 17:40 UTC. During this measurement, the solar zenith angle was about 45°, the sky was clear, and the surface wind speed was about 11 m s^{-1}. The RADCAM instrument operates at the wavelength of 555 (±20) nm. The dynamic downwelling radiance field from 0.68 m to 1.45 m below surface was measured at a sampling rate of 4 Hz and an integration time of 0.02 s. Here we are comparing against the results at 1 m. To compare with these data, we use the atmospheric and oceanic optical properties at the wavelength of 532 nm as described above, the high-sea situation (wind speed of 9.3 m s^{-1}), and a solar zenith angle of 45°. These input parameters are generally consistent with those during the radiance field measurement. Figures 11a and 11b show the comparison between the measured and simulated, respectively, underwater downwelling radiance fields in units of W m^{-2} nm^{-1} sr^{-1}. The measured radiance is slightly higher than the simulation (a larger high radiance region, and brighter in the Snell's cone). Possible sources of this discrepancy include slight differences in the solar irradiance, the atmospheric and oceanic optical properties at the two wavelengths, the difference between the measured water IOPs that were used in the model simulation and those when the light field measurement was performed, and uncertainties associated with the aerosol model. Despite this discrepancy, the simulation did give dynamic features (such as distortions of the Snell's cone and fine structures at the edge of the Snell's cone) that are qualitatively similar to those seen in the measurement. The measured light field features far more pronounced fine structures and a more distorted Snell's cone (almost one-third of the high radiance region is outside the flat-surface Snell's cone). The sources of this discrepancy are twofold: 1. the instantaneous wave slope field above the measured light field is different from the wave slope measurement used in the model simulation; 2. the model neglected wave elevations, which play an important role in determining the overall distortion of the Snell's cone.

5. Discussions and Conclusions

[50] As part of the Radiance in a Dynamic Ocean project, we have developed a vector radiative transfer model to predict the polarized light field immediately under highly dynamic ocean surfaces. A hybrid of the matrix operator and Monte Carlo radiative transfer models, the developed model is optimized for simulations of the light field in a dynamic atmosphere-surface-ocean system, where the temporal variations are primarily limited in the surface layer while the atmosphere and ocean layers can be treated statically.

[51] This model is computationally fast for simulating temporal variations in the underwater downwelling light field with sufficiently high spatial- and angular-resolution including the full polarization state. For results reported in this study, the simulations were performed on an IBM Cluster 1600 based on IBM's Power5+ processors running at 1.9 GHz. The hybrid model was implemented in Fortran 90 and parallelized using Message Passing Interface (MPI). When running on 128 processors (8 nodes and 16 processors per node), the wall times for the calculations of the atmospheric and oceanic impulse-response functions are about 4 min for $\mathbf{T}_{01,\mathrm{eff}}$, 15 min for $\mathbf{D}_{2d}^{\mathrm{diff}}$, and 1 h for $\mathbf{R}_{23}$, and the wall time for the matrix operator calculation of each instantaneous frame is about 4 min. It becomes obvious that the hybrid model is very efficient for calculations of dynamic light fields, which share the same atmospheric and oceanic

impulse-response functions but have different interface impulse-response functions.

[52] Model simulations can act as a bridge to connect and test vast amounts of field data collected during RaDyO experiments. Using measured water inherent optical properties and wave slope fields, the hybrid model has been shown to be capable of generating underwater downwelling polarized light fields qualitatively comparable with measurements of underwater polarized light field. However, these field data were not exactly synchronized or collocated, and a quantitative frame-by-frame comparison between modeled and measured light field was not possible. The performance of the hybrid model may be further tested should such data sets become available. The discrepancy between the simulated and measured light field may also come from the fact that the model only considers wave slopes but not wave elevations, which is important for some of the dynamic features in the light field such as wave focusing. Inclusion of wave elevations into the model will be reported in future studies.

[53] Simulation results from the hybrid model have implications to both measurement and simulation of the underwater light field. It is shown that given appropriate wave slope and ocean optical property measurements, model simulation does a better job in giving a comprehensive understanding of the dynamic underwater light field, including its spatial, angular, and temporal distributions. Specifically, it is demonstrated that, using appropriate surface measurements, model simulations of underwater light fields can reach a higher temporal resolution than measurements do. Model-simulations can also provide guidelines in understanding and interpreting measurements of the dynamic underwater light field made by instruments with limited spatial, angular, or temporal resolution. Simulation results involving an instantaneous wave slope field for the air-sea interface suggested that the edge of the Snell's cone in an instantaneous light field is not as blurred as what conventional model simulations using the statistical Cox-Munk wave slope model would predict when the surface wind speed increases. It becomes consistent with Cox-Munk predictions only after spatial- and/or temporal-averages are considered [see, e.g., *You et al.*, 2009]. Therefore, caution should be used in determining which wave model to use based on the situation of interest.

Notation

a absorption coefficient, m^{-1}.
b scattering coefficient, m^{-1}.
c extinction coefficient, m^{-1}.
d depth of detector below air-sea interface, m.
DoP degree of (linear) polarization, dimensionless.
$\mathbf{D}$ detector response function, dimensionless.
I radiance, W m^{-2} nm^{-1} sr^{-1}.
$\mathbf{I}$ Stokes vector, whose elements are in units of W m^{-2} nm^{-1} sr^{-1}.
$\mathbf{n}$ direction determined by zenith and azimuth angles.
$\mathbf{r}$ position in the horizontal dimension.
$\mathbf{R}$ reflection response function, dimensionless.
$\mathbf{T}$ transmission response function, dimensionless.
z wave elevation, m.
λ wavelength, nm.
τ optical depth, dimensionless.
ω single scattering albedo, dimensionless.
χ orientation of the electric field vector, degree.

[54] **Acknowledgments.** Y. You and G. W. Kattawar were supported by the Office of Naval Research (ONR) Radiance in a Dynamic Ocean (RaDyO) program under contract N00014-06-1-0069. K. Voss and P. Bhandari are supported by the ONR under contract N00014-11-1-0153. M.R. Lewis and J. Wei were supported by ONR under contract N00014-09-C-0084. C.J. Zappa was supported by the ONR RaDyO program under contract N00014-06-1-0372. Howard Schultz was with support by the ONR RaDyO program under contract N00014-07-1-0010 and an ONR DURIP award under contract N00014-07-1-0731A00001.

References

Adams, C. N., and G. W. Kattawar (1970), Solutions of equations of radiative transfer by an invariant imbedding approach, *J. Quant. Spectrosc. Radiat. Transfer*, *10*(5), 341–356, doi:10.1016/0022-4073(70)90101-9.

Adams, J. T., E. Aas, N. K. Hojerslev, and B. Lundgren (2002), Comparison of radiance and polarization values observed in the Mediterranean Sea and simulated in a Monte Carlo model, *Appl. Opt.*, *41*(15), 2724–2733, doi:10.1364/AO.41.002724.

Bartlett, J. S., K. J. Voss, S. Sathyendranath, and A. Vodacek (1998), Raman scattering by pure water and seawater, *Appl. Opt.*, *37*(15), 3324–3332, doi:10.1364/AO.37.003324.

Chandrasekhar, S. (1960), *Radiative Transfer*, Dover, New York.

Chang, G., M. S. Twardowski, Y. You, M. Moline, P.-W. Zhai, S. Freeman, M. Slivkoff, F. Nencioli, and G. W. Kattawar (2010), Platform effects on optical variability and prediction of underwater visibility, *Appl. Opt.*, *49*(15), 2784–2796, doi:10.1364/AO.49.002784.

Cox, C., and W. Munk (1954), Statistics of the sea surface derived from Sun glitter, *J. Mar. Res.*, *13*(2), 198–227.

Cronin, T. W., and N. Shashar (2001), The linearly polarized light field in clear, tropical marine waters: Spatial and temporal variation of light intensity, degree of polarization and e-vector angle, *J. Exp. Biol.*, *204*(14), 2461–2467.

Darecki, M., D. Stramski, and M. Sokolski (2011), Measurements of high-frequency light fluctuations induced by sea surface waves with an Underwater Porcupine Radiometer System, *J. Geophys. Res.*, doi:10.1029/2011JC007338, in press.

Fournier, G. R., and J. L. Forand (1994), Analytic phase function for ocean water, in *Ocean Optics XII*, edited by J. S. Jaffe, *Proc. SPIE Int. Soc. Opt. Eng.*, 2258, 194–201.

Hansen, J. E., and L. D. Travis (1974), Light scattering in planetary atmospheres, *Space Sci. Rev.*, *16*, 527–610, doi:10.1007/BF00168069.

He, X., Y. Bai, Q. Zhu, and F. Gong (2010), A vector radiative transfer model of coupled ocean-atmosphere system using matrix-operator method for rough sea-surface, *J. Quant. Spectrosc. Radiat. Transfer*, *111*(10), 1426–1448, doi:10.1016/j.jqsrt.2010.02.014.

Hedley, J. (2008), A three-dimensional radiative transfer model for shallow water environments, *Opt. Express*, *16*, 21,887–21,902, doi:10.1364/OE.16.021887.

Ivanoff, A., N. Jerlov, and T. H. Waterman (1961), A comparative study of irradiance, beam transmittance and scattering in the sea near Bermuda, *Limnol. Oceanogr.*, *6*(2), 129–148, doi:10.4319/lo.1961.6.2.0129.

Jin, Z. H., T. P. Charlock, K. Rutledge, K. Stamnes, and Y. J. Wang (2006), Analytical solution of radiative transfer in the coupled atmosphere-ocean system with a rough surface, *Appl. Opt.*, *45*(28), 7443–7455, doi:10.1364/AO.45.007443.

Kattawar, G. W., and C. N. Adams (1989), Stokes vector calculations of the submarine light-field in an atmosphere-ocean with scattering according to a Rayleigh phase matrix: Effect of interface refractive-index on radiance and polarization, *Limnol. Oceanogr.*, *34*(8), 1453–1472, doi:10.4319/lo.1989.34.8.1453.

Kattawar, G. W., G. N. Plass, and F. E. Catchings (1973a), Matrix operator theory of radiative transfer. 2: Scattering from maritime haze, *Appl. Opt.*, *12*(5), 1071–1084, doi:10.1364/AO.12.001071.

Kattawar, G. W., G. N. Plass, and J. A. Guinn Jr. (1973b), Monte Carlo calculations of the polarization of radiation in the Earth's atmosphere-ocean system, *J. Phys. Oceanogr.*, *3*, 353–372, doi:10.1175/1520-0485(1973)003<0353:MCCOTP>2.0.CO;2.

Lenoble, J., and C. Broquez (1984), A comparative review of radiation aerosol models, *Contrib. Atmos. Phys.*, *57*, 1–20.

Miyamoto, K. (1964), Fish-eye lens, *J. Opt. Soc. Am.*, *54*, 1016–1061.

Mobley, C. D. (1994), *Light and Water: Radiative Transfer in Natural Waters*, Academic, San Diego, Calif.

Mobley, C. D., and L. K. Sundman (2000), HydroLight 4.1 Users' Guide, Sequoia Sci., Inc., Redmond, Wash. [Available at http://www.sequoiasci.com.)

Plass, G. N., G. W. Kattawar, and F. E. Catchings (1973), Matrix operator theory of radiative transfer. 1: Rayleigh scattering, *Appl. Opt.*, *12*(2), 314–329, doi:10.1364/AO.12.000314.

Plass, G. N., G. W. Kattawar, and J. A. Guinn (1975), Radiative transfer in the earth's atmosphere and ocean: Influence of ocean waves, *Appl. Opt.*, *14*(8), 1924–1936, doi:10.1364/AO.14.001924.

Pope, R. M., and E. S. Fry (1997), Absorption spectrum (380–700 nm) of pure water. 2. Integrating cavity measurements, *Appl. Opt.*, *36*(33), 8710–8723, doi:10.1364/AO.36.008710.

Sabbah, S., and N. Shashar (2006), Underwater light polarization and radiance fluctuations induced by surface waves, *Appl. Opt.*, *45*(19), 4726–4739, doi:10.1364/AO.45.004726.

Sabbah, S., and N. Shashar (2007), Light polarization under water near sunrise, *J. Opt. Soc. Am. A*, *24*(7), 2049–2056, doi:10.1364/JOSAA.24.002049.

Sabbah, S., A. Barta, J. Gál, G. Horváth, and N. Shashar (2006), Experimental and theoretical study of skylight polarization transmitted through Snell's window of a flat water surface, *J. Opt. Soc. Am. A*, *23*(8), 1978–1988, doi:10.1364/JOSAA.23.001978.

Shashar, N., S. Sabbah, and T. W. Cronin (2004), Transmission of linearly polarized light in seawater: Implications for polarization signaling, *J. Exp. Biol.*, *207*(20), 3619–3628, doi:10.1242/jeb.01187.

Smith, R., and K. Baker (1981), Optical-properties of the clearest natural-waters (200–800 nm), *Appl. Opt.*, *20*(2), 177–184, doi:10.1364/AO.20.000177.

Timofeeva, V. A. (1974), Optics of turbid waters (Results of laboratory studies), in *Optical Aspects of Oceanography*, edited by N. Jerlov and E. Nielsen, pp. 177–219, Academic, London.

Tonizzo, A., J. Zhou, A. Gilerson, M. S. Twardowski, D. J. Gray, R. A. Arnone, B. M. Gross, F. Moshary, and S. A. Ahmed (2009), Polarized light in coastal waters: Hyperspectral and multiangular analysis, *Opt. Express*, *17*(7), 5666–5682, doi:10.1364/OE.17.005666.

van de Hulst, H. C. (1981), *Light Scattering by Small Particles*, Dover, New York.

van Dommelen, R., M. Lewis, and J. Wei (2010), Instrumentation, calibration and validation of a high-dynamic-range radiance camera, paper presented at Ocean Optics XX, Oceanogr. Soc., Anchorage, Alaska.

Voss, K. J., and E. S. Fry (1984), Measurement of the Mueller matrix for ocean water, *Appl. Opt.*, *23*(23), 4427–4439, doi:10.1364/AO.23.004427.

Voss, K. J., P. Bhandari, and L. Logan (2008) A new spectral polarized radiance distribution camera system, DPOL, paper presented at Ocean Optics X1X, Oceanogr. Soc., Barca, Italy, Oct.

Waterman, T. H. (1954), Polarization patterns in submarine illumination, *Science*, *120*(3127), 927–932, doi:10.1126/science.120.3127.927.

Waterman, T. H., and W. E. Westell (1956), Quantitative effects of the Sun's position on submarine light polarization, *J. Mar. Res.*, *15*, 149–169.

You, Y., P.-W. Zhai, G. W. Kattawar, and P. Yang (2009), Polarized radiance fields under a dynamic ocean surface: A three-dimensional radiative transfer solution, *Appl. Opt.*, *48*(16), 3019–3029, doi:10.1364/AO.48.003019.

You, Y., D. Stramski, M. Darecki, and G. W. Kattawar (2010), Modeling of wave-induced irradiance fluctuations at near-surface depths in the ocean: A comparison with measurements, *Appl. Opt.*, *49*(6), 1041–1053, doi:10.1364/AO.49.001041.

Zappa, C. J., M. L. Banner, H. Schultz, A. Corrada-Emmanuel, L. B. Wolff, and J. Yalcin (2008), Retrieval of short ocean wave slope using polarimetric imaging, *Meas. Sci. Technol.*, *19*(5), 055503, doi:10.1088/0957-0233/19/5/055503.

Zhai, P.-W., G. W. Kattawar, and P. Yang (2008a), Impulse response solution to the three-dimensional vector radiative transfer equation in atmosphere-ocean systems. I. Monte Carlo method, *Appl. Opt.*, *47*(8), 1037–1047, doi:10.1364/AO.47.001037.

Zhai, P.-W., G. W. Kattawar, and P. Yang (2008b), Impulse response solution to the three-dimensional vector radiative transfer equation in atmosphere-ocean systems. II. The hybrid matrix operator-Monte Carlo method, *Appl. Opt.*, *47*(8), 1063–1071, doi:10.1364/AO.47.001063.

Zhai, P.-W., Y. X. Hu, J. Chowdhary, C. R. Trepte, P. L. Lucker, and D. B. Josset (2010), A vector radiative transfer model for coupled atmosphere and ocean systems with a rough interface, *J. Quant. Spectrosc. Radiat. Transfer*, *111*(7–8), 1025–1040, doi:10.1016/j.jqsrt.2009.12.005.

P. Bhandari and K. J. Voss, Department of Physics, University of Miami, 1320 Campo Sano Dr., Coral Gables, FL 33124, USA.

G. W. Kattawar and Y. You, Department of Physics and Astronomy, Texas A&M University, College Station, TX 77843-4242, USA. (kattawar@tamu.edu; youyu3@gmail.com)

M. Lewis and J. Wei, Department of Oceanography, Dalhousie University, 1355 Oxford St., Halifax, NS B3H 4R2, Canada.

H. Schultz, Department of Computer Science, University of Massachusetts, 140 Governors Dr., Amherst, MA 01003, USA.

C. J. Zappa, Ocean and Climate Physics Division, Lamont-Doherty Earth Observatory, Columbia University, 61 Route 9W, Palisades, NY 10964, USA.